Phase-matching effects in the generation of high-energy photons by mid-infrared few-cycle laser pulses

2011 New J. Phys. 13 073003

(http://iopscience.iop.org/1367-2630/13/7/073003)

New Journal of Physics
The open-access journal for physics

Phase-matching effects in the generation of high-energy photons by mid-infrared few-cycle laser pulses

C Vozzi[1,5], M Negro[2], F Calegari[2], S Stagira[2], K Kovács[3,4] and V Tosa[3]

[1] CNR-IFN, 20133 Milan, Italy
[2] Department of Physics, Politecnico di Milano, 20133 Milan, Italy
[3] National Institute for R&D on Isotopic and Molecular Technologies, 400293 Cluj-Napoca, Romania
[4] Department of Optics and Quantum Electronics, University of Szeged, H-6701 Szeged, Hungary
E-mail: caterina.vozzi@polimi.it

New Journal of Physics **13** (2011) 073003 (17pp)
Received 8 February 2011
Published 5 July 2011
Online at http://www.njp.org/
doi:10.1088/1367-2630/13/7/073003

Abstract. We report on our experimental and theoretical investigations on the generation of high-order harmonics driven by 1500 nm few-cycle laser pulses in xenon. In contrast to the common belief, we found experimental evidence suggesting that harmonic generation driven by mid-infrared laser pulses can be realized with high efficiency; in particular, an enhancement of very high harmonic orders can be achieved under suitable conditions of the laser–medium interaction. The experimental results were simulated by a 3D non-adiabatic model. The theoretical outcomes confirm the experimental findings and provide a physical explanation for the counter-intuitive results. In particular, a time-dependent phase-matching analysis threw light on the generation mechanisms at a timescale of half optical cycle of the fundamental pulse.

[5] Author to whom any correspondence should be addressed.

Contents

1. Introduction

High-order harmonic generation (HHG) is a widespread technique exploited for the production of coherent extreme ultraviolet (XUV) radiation, which can then be used for biological and molecular imaging, spectroscopy, etc. This process can be understood in the framework of the three-step model [1]: the strong laser field tunnel ionizes the outermost electron of the target atom; the photoelectron is then accelerated in the continuum and driven back to the parent ion by the laser field; afterwards, it recollides with the ion, emitting the acquired energy in a radiation burst. Since this emission is repeated every half optical cycle of the driving pulse, the emitted spectrum appears as a comb of odd harmonics of the fundamental frequency. The cutoff of the high-harmonic (HH) spectrum (in atomic units) is $I_p + 3.17U_p$ [1], where I_p is the ionization potential and $3.17U_p \sim 0.58I/(4\omega_0^2)$ is the maximum kinetic energy of the recombining electron, which depends on the laser field intensity I and on the laser frequency ω_0 expressed in atomic units. The ponderomotive energy U_p can be increased (i.e. the cutoff can be extended) by increasing the intensity I and/or increasing the wavelength λ_0 of the incident pulse. Very-high-intensity laser pulses have serious drawbacks when applied to media of low ionization potential, because they cause fast ionization depletion. Increasing the driving wavelength seems to be more convenient, and in the past, several groups have constructed HHG experiments operating with mid-infrared (mid-IR) pulses [2–7]. On the other hand, it has also been shown that the harmonic yield decreases as λ_0^{-k} with $5.5 < k < 6.5$ [8, 9]. If one aims at efficient HHG driven by ultrashort pulses with wavelengths longer than the widely used 800 nm, one has to cope with this steep decrease of the harmonic yield. Furthermore, macroscopic phenomena affecting the pulse propagation in ionizing media, such as self-phase modulation (SPM) and distortion of the beam's spatial profile, become particularly important at mid-IR wavelengths. Several strategies have been proposed for overcoming such problems with mid-IR drivers: for example, HHG in loose focusing geometry at low ionization levels [10]; generation of phase-matched harmonics in hollow waveguides [11]; and HHG by multicolour drivers, i.e. mixing the fundamental mid-IR driver with shorter-wavelength pulses [12].

In this paper, we will show that, in contrast to the common belief, a high ionization level in the interaction medium can create such circumstances where harmonic yield can be significantly improved for high-energy photons. In particular when HHG is performed with a mid-IR pulse of

high energy, the effects of the plasma produced in the interaction volume are dominant and can produce unexpected results. These effects are not necessarily destructive, but can be efficiently exploited in order to increase the emission yield for HH orders.

We will focus on the discussion of different configurations of good phase-matching (PM) that arise as a consequence of the propagation of an intense IR few-cycle pulse in an ionizing medium. Finding an optimal focusing geometry for this purpose is not trivial. A specific feature of HHG driven by high-intensity laser pulses is the strong SPM of the pulse during propagation in the ionizing media. The non-trivial (temporal) phase modulation contributes to the PM scheme and determines the occurrence of favourable PM conditions. In this paper, we show that, due to the strong SPM, good PM is restricted to a few half optical cycles within the driving pulse, leading to a strong harmonic emission in a narrow temporal window.

We will also demonstrate, both experimentally and by numerical calculations, that one can use intense mid-IR few-cycle pulses to efficiently obtain strong coherent XUV radiation by HHG in Xe. Good harmonic yield can be achieved despite the well-known fact that the yield decays rapidly as the laser wavelength increases. The reason for the high yield of the harmonic signal is that at longer wavelengths the effects of pulse propagation in noble gas medium become very important, but such effects can induce good PM conditions and can contribute to the enhancement of the harmonic signal.

This paper is organized as follows. In section 2 we describe the experimental setup used for measurements; the experimental outcomes are then presented in section 3; afterwards, in section 4 we introduce the theoretical model implemented for the interpretation of the measured harmonic spectra. In section 5, we compare the theoretical predictions obtained from simulations with the experimental results; in this section, we discuss in more detail several features of the PM mechanism found in our experiments. The model described briefly in section 4 is suitable to gain a deeper insight into the investigated phenomena on a timescale of half optical cycle, and as such, it is a useful tool for physical interpretation of the experiments. Finally, we conclude and provide an outlook for future work.

2. Experimental setup

To generate high-order harmonics, we exploited a mid-IR parametric source pumped by an amplified Ti:sapphire laser system (800 nm, 60 fs, 12 mJ and 10 Hz). The mid-IR source produces few-cycle carrier-envelope phase (CEP) stabilized pulses with an energy of 1.6 mJ and a carrier wavelength tunable between 1.4 and 1.8 μm [13]. This source is based on intra-pulse difference frequency (DF) generation: a small portion of the 800 nm laser pulse is used for the generation of a broad continuum by filamentation in a krypton-filled gas cell followed by compression with chirped mirrors. DF is produced between the short- and long-wavelength portions of this continuum in a β-barium borate (BBO) crystal. The energy of this DF seed is then increased up to the mJ level by means of a two-stage optical parametric amplifier (OPA) based on BBO in type II PM configuration pumped by the remaining 800 nm laser pulse. The amplified DF pulses have a nearly transform-limited duration of about 18 fs without the use of any compression system, because the OPAs present zero dispersion around 1.5 μm in this PM configuration. By changing the PM angles in the OPAs it is also possible to tune the carrier wavelength of the amplified pulses between 1.4 and 1.8 μm without significantly affecting pulse duration and energy. These pulses are also intrinsically CEP stabilized with a residual rms fluctuation of the order of 200 mrad [14].

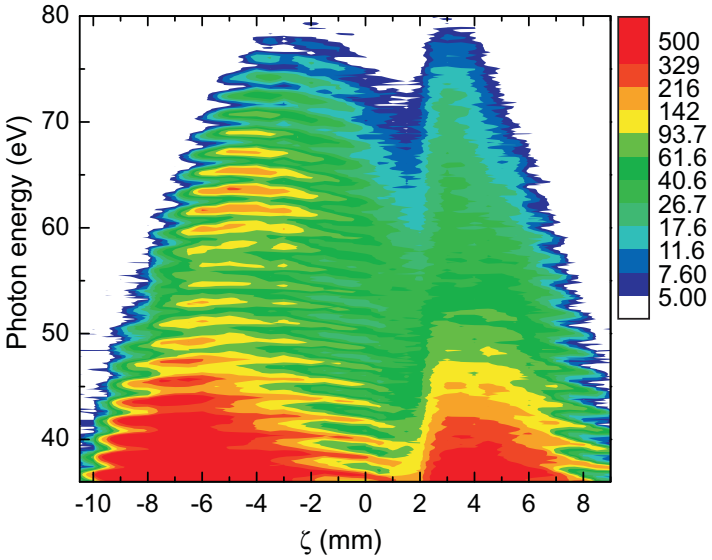

Figure 1. Harmonic spectra measured in Xe as a function of emitted photon energy and position ζ of the medium with respect to the nominal focus.

HHG is realized in a vacuum chamber by focusing the mid-IR parametric pulses on a synchronized gas jet (Xe at a backing pressure of 3.5 bar) by means of a spherical mirror with 20 cm focal length. In order to control the focusing condition, we used an adjustable iris for clipping the driving beam. The position of the pulsed gas jet can be finely three-dimensional (3D)-controlled by means of three stepping motors under vacuum with a minimum step size of 5 μm along the laser propagation direction and of 0.1 μm in the plane perpendicular to it. The harmonic radiation, passing through a 1 mm diameter pinhole placed 150 mm downstream of the interaction region, is analysed with a flat-field XUV spectrometer equipped with a toroidal mirror and a concave variable-line-spacing grating. The XUV radiation is detected by a micro-channel plate coupled to a CCD camera. The XUV spectrometer operates between 35 and 200 eV; the efficiency of the detection system has been characterized in such a spectral region and it was taken into account in the acquired measurements.

3. Experimental results

Figure 1 shows the experimental harmonic spectra acquired in xenon as a function of the emitted XUV photon energy and of the position ζ of the medium with respect to the nominal focus; positive values of ζ correspond to a location of the gas jet downstream of the laser focus. There are several features that can be easily perceived: (i) one can observe two regions of maximum cutoff extension (up to 80 eV), a larger one around $\zeta = -4$ mm and a smaller one around $\zeta = 4$ mm; the harmonic structure is well defined in the first region, whereas it is smoothed in the second one. It will be shown in the following that the two different regions we observed are ascribed to different PM mechanisms acting in the gas jet, respectively favouring long and short electron trajectories during HH generation. (ii) A strong reduction of the XUV signal is observed in the region around the nominal focus of the laser beam; this feature is in general expected, owing to the combined action of several phase-mismatch effects. (iii) The

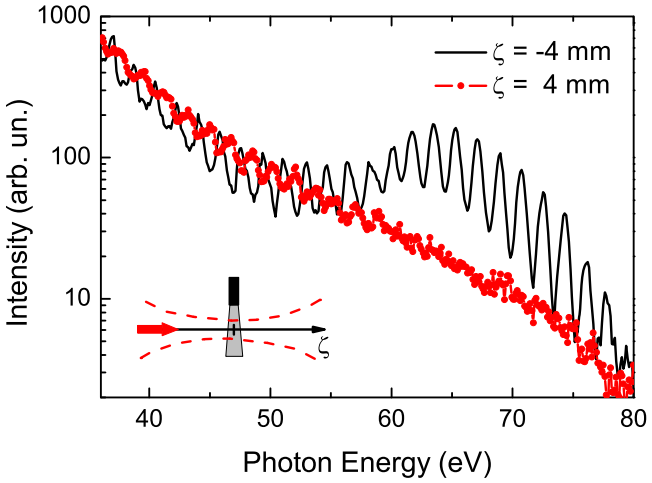

Figure 2. Harmonic spectra measured in Xe at the medium positions $\zeta = -4$ mm (black solid line) and $\zeta = 4$ mm (red line with symbols) with respect to the nominal focus. The inset shows the scheme of the laser focusing conditions.

position of the harmonic peaks is not constant along the scan, but changes with ζ; this effect has been already observed in the past with Ti:sapphire driving pulses [15]. (iv) A region of XUV enhancement is observed around 65 eV for negative values of ζ; we will show that this feature can be ascribed to propagation effects.

The major differences between the two mentioned regions are seen more clearly in figure 2, where the HH spectra acquired at $\zeta = -4$ mm (black solid line) and $\zeta = 4$ mm (red line with symbols) are compared. As can be seen from the figure, the XUV enhancement observed around 65 eV for $\zeta = -4$ mm amounts to about an order of magnitude with respect to the other position. It is worth noting that the cutoff extension in the two cases is comparable; hence, the peak intensity reached by the driving pulse in these two positions is almost the same. As a further note, we point out that the emission yield in the two cases is almost the same at low harmonic orders.

The occurrence of an XUV enhancement at HHs has important consequences both in the application of XUV radiation and in the understanding of the physics of HHG. In particular, a proper choice of the focusing conditions and of the position of the generating medium allows for a noticeable increase in the emission yield on a photon energy range which is of major importance in attosecond science [16].

On the other hand, the spectral modulation observed at $\zeta = -4$ mm can be attributed to propagation effects, since the same feature is absent in the opposite position of the generating medium. This finding emphasizes the essential role of PM in the generation of high-order harmonics. In particular under our experimental conditions, we expect that PM plays a major role in determining the characteristics of the emitted XUV radiation because of the thickness of the generating medium (which is estimated in our case to be about 1.5 mm) and because of the relatively long focal length. To exploit HHG for atomic or molecular spectroscopy, the experimental configuration should be carefully chosen in order to minimize PM effects.

4. Theoretical model

4.1. Simulation methods

In order to explain the features observed in these experiments, we performed intensive numerical calculations using a 3D non-adiabatic model [17, 18]. The model solves sequentially three distinct aspects of the generation as follows:

1. Propagation of the driving field $E(r, z, t)$ through the medium:

$$\nabla^2 E(r, z, t) - \frac{1}{c^2}\frac{\partial^2 E(r, z, t)}{\partial t^2} = \frac{\omega^2}{c^2}\left(1 - \eta_{\text{eff}}^2\right) E(r, z, t). \tag{1}$$

   In this wave equation, η_{eff} is the effective refractive index of the medium,

$$\eta_{\text{eff}}(r, z, t) = \eta_0 + \eta_2 I(r, z, t) - \frac{\omega_{\text{p}}^2(r, z, t)}{2\omega^2}, \tag{2}$$

   where $\eta_0 = 1 + \delta_1 + \mathrm{i}\beta_1$ accounts for refraction and absorption, the second term includes the optical Kerr effect and, finally, the third term accounts for the presence of n_{e} density of electrons through the plasma frequency $\omega_{\text{p}} = \sqrt{4\pi e^2 n_{\text{e}}/m}$. The ionization rate is calculated using the Ammosov–Delone–Krainov (ADK) model.

2. The response of a single atom to the driving field estimated within the strong field approximation [19]:

$$P_{\text{nl}}(t) = 2\text{Re}\left\{\mathrm{i}\int_{-\infty}^{t} \mathrm{d}t' d^*[p_{\text{st}}(t', t) - A(t)]E(t')\exp\left[-\int_{-\infty}^{t'} w(t'')\mathrm{d}t''\right]\right.$$
$$\left.\times \exp\left[-\mathrm{i}S_{\text{st}}(t', t)\right] d\left[p_{\text{st}}(t', t) - A(t)\right]\right\}[n_0 - n_{\text{e}}(t)], \tag{3}$$

   where $P_{\text{nl}}(t)$ is the nonlinear polarization, t' and t are the photoelectron ionization and recombination times, respectively, $A(t)$ is the vector potential associated with the driving field, $w(t)$ is the tunnel ionization rate, p_{st} is the stationary electron momentum and S_{st} is the corresponding stationary action [19], d is the dipole term corresponding to the bound–continuum transition and n_0 and n_{e} are the initial atomic density and the time-dependent free electron density, respectively.

3. Propagation of the harmonic field $E_{\text{h}}(r, z, t)$ through the medium:

$$\nabla^2 E_{\text{h}}(r, z, t) - \frac{1}{c^2}\frac{\partial^2 E_{\text{h}}(r, z, t)}{\partial t^2} = \mu_0 \frac{\partial^2 P_{\text{nl}}(r, z, t)}{\partial t^2}. \tag{4}$$

   Any realistic modelling of HHG should consider these three aspects, because propagation through the ionizing medium induces modifications in space and time of the original laser field and the single-atom response will be directly affected by these modifications. Finally, harmonic field propagation must be considered, accounting not only for the PM effects but also for the dispersion and absorption of the HH field in the medium.

   To better model the physical process, we have also taken into account the focusing geometry of the driving field as well as the optical configuration used for collecting the harmonics. In particular, we measured the pulse energy and beam profile at the entrance of

the experimental chamber and used them as the input data. We used the diffraction integral to estimate the field at medium entrance, thus accounting for the truncation of the laser beam at the input iris and for the focusing configuration. To calculate the far field, we used the Hankel transform including the effect of the 1 mm diameter pinhole placed between the interaction region and the XUV spectrometer.

The experimental conditions described in section 2 have been used as the input data in the numerical simulations. Thus, the basic parameters were the following: a truncated Gaussian laser beam of 0.3 mJ energy, 20 fs duration and 1500 nm wavelength is focused with a 20 cm focal length mirror into a Xe gas jet. From the experimental backing pressure of 3.5 bar, we estimated 20 torr pressure in the interaction region [22], which is assumed to be 1.5 mm long.

4.2. Phase-matching calculation

Time-dependent PM analysis was also performed in order to complete the data description. A somewhat natural extension of the static vector model of Balcou *et al* for PM [20] to a time-dependent version has been proposed by Tosa *et al* [21]. The condition for perfect PM is obtained when the wavevector of the qth harmonic $\mathbf{k}_q$ equals the dipole wavevector $\mathbf{k}_{\rm pol}$, which can be written as

$$\begin{aligned}\mathbf{k}_q = \mathbf{k}_{\rm pol} &= q\nabla\varphi_0(r,z,t) - \nabla\Phi_{\rm at}(r,z,t)\\ &= q\left\{(2\pi/\lambda)\mathbf{e}_z + \nabla\arg[E(r,z,t)]\right\} + \nabla\alpha I(r,z,t),\end{aligned} \tag{5}$$

where the phase of the driving field $\varphi_0(r,z,t)$ and the average intensity $I(r,z,t)$ in one optical cycle are calculated from the propagated field, e.g. from the solution of the propagation equation. Here we assumed that the phase accumulated by the electron during the excursion in the field $\Phi_{\rm at}(r,z,t)$ is proportional to the average intensity, α being the proportionality factor. The PM condition is quantified through the phase mismatch, $\delta k(t) = 2\pi q/\lambda - |\mathbf{k}_{\rm pol}(t)|$, and the coherence length, $L_{\rm coh} = \pi/\delta k(t)$. During the calculations, we consider that there is good PM condition when the coherence length is comparable to the total length of the interaction region.

Taking into account the negative value of the constant α in (5), we observe that HHG under PM conditions happens when both the phase of the fundamental pulse and the intensity of the propagated beam vary in the same direction. As is well known, such a condition is fulfilled, for example, in a Gaussian beam, on-axis and after the focus, when both the phase and intensity decrease along the propagation direction. When the gas medium is placed before the focus, the PM condition is only fulfilled in restricted regions off-axis where the phase and intensity gradients in the radial direction become important. We will show that this already classical picture changes completely when including propagation effects.

5. Discussion

The measured harmonic spectra are again shown in figure 3(a), where they are compared to the computed HH spectra in far field and in near field, which are displayed in figures 3(b) and (c), respectively.

The measured data show three regions where the harmonic emission is enhanced. They are labelled as L, S and C according to the kind of trajectories that found good PM conditions as will be discussed in the following. The L and C regions are well reproduced in the calculated

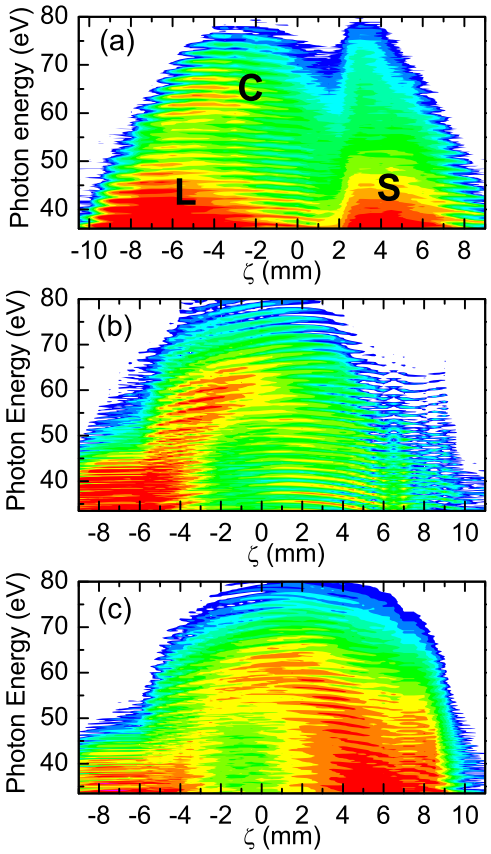

Figure 3. Harmonic spectra in Xe shown as a function of emitted photon energy and position ζ of the medium with respect to the nominal focus. The experimental results (a) are compared with the outcomes of the numerical simulations, computed in the experimental conditions in the far field (b) and in the near field (c), respectively. The letters L, S and C reported in panel (a) refer to different PM conditions, as discussed in the main text.

far field, whereas the S region can be seen in the calculated near field. All three sets of results exhibit a central ζ-domain, roughly from $\zeta = -2$ to $\zeta = 2$ mm, where the harmonic field is weak for the spectral range up to 50 eV. The harmonic field above 50 eV is instead amplified when the gas medium is situated from $\zeta = -6$ to $\zeta = -2$ mm.

We start the analysis of the numerical results by inspecting the laser field configuration over the interaction region, as this can provide information about the HH generation process. Such a result is shown in figure 4(a) where we plotted the propagated on-axis intensity of the driving field for different ζ positions of the 1.5 mm-long medium. While the low initial intensities keep the beam almost unperturbed, the cases close to the focal region show strong propagation effects. After a slight increase the intensity exhibits a strong decrease owing to plasma defocusing. As seen in figure 4(b), where we show the ionization fraction produced by the fields in figure 4(a), we have full ionization on-axis for ζ between -2 and 6 mm, and this full ionization remains for most of the propagation distance. The depletion of the medium is in part responsible for the gap observed in the HH intensity shown in figure 3 when the medium is placed in the central part of the beam.

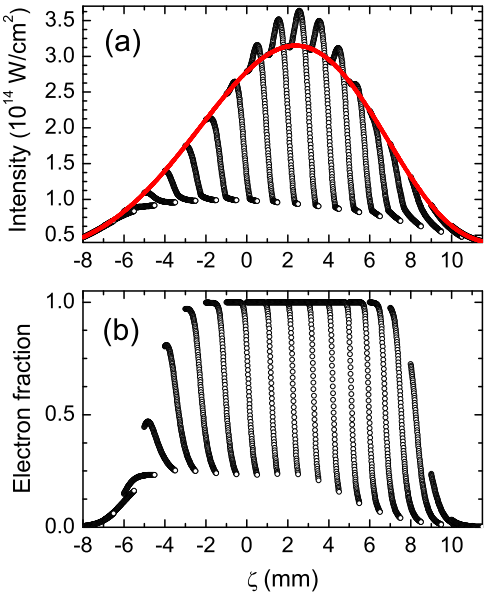

Figure 4. (a) The on-axis intensity (black open symbols) along the propagation direction for different ζ positions of the medium with respect to the beam. Each continuous set of open symbols represents one jet position. The red curve represents the value of on-axis intensity for the propagation in vacuum of the driving field. (b) Corresponding electron fractions. The medium is assumed to be 1.5 mm long in each case.

In order to have a complete representation of the spatial propagation effects, we present in figure 5 the field configurations for three different positions of the jet. One can see that the dominant feature of the propagation is the defocusing of the beam due to electron plasma. Indeed, we found that the plasma contribution to the refractive index is dominant over dispersion by the neutrals and Kerr contribution. However, the spatial configuration is strongly affected also by the position of the jet relative to the focus. The upper ($\zeta = -2$ mm) and lower ($\zeta = 6$ mm) panels in this plot are chosen to have approximately the same initial radial profile of the intensity. The two cases generate the same plasma density; however, the configurations are different due to the initial front curvature of the beam. It is known that the ionization profile formed initially when the pulse enters the gas medium acts like a diverging lens with decreasing focal power as r increases. Therefore the initial convergent wavefront changes its radius of curvature more in the central and less in the peripheral regions. In particular, this radius of curvature becomes infinite [23] when the variation of the refractive index along the radial direction satisfies the equation $\delta n = \lambda^2/(2\pi^2 w_0^2)$, where λ and w_0 denote the wavelength and waist of the incoming beam. The consequence of this is the formation of a flat radial profile, which was confirmed experimentally either by plasma measurements of both the longitudinal and transversal beam profiles [18, 24] or by direct measurement of the beam profile [25].

As is evident from figure 5, the flat beam profile occurs in all three cases; however, the regime of propagation is different with obvious consequences for HH generation. When the flattening happens in an initially converging beam ($\zeta = -2$ mm), the flat profile propagates over longer distances as the divergence due to plasma is compensated for with focusing. This is one of the specific features of the propagation process of mid-IR pulses: owing to the strong plasma

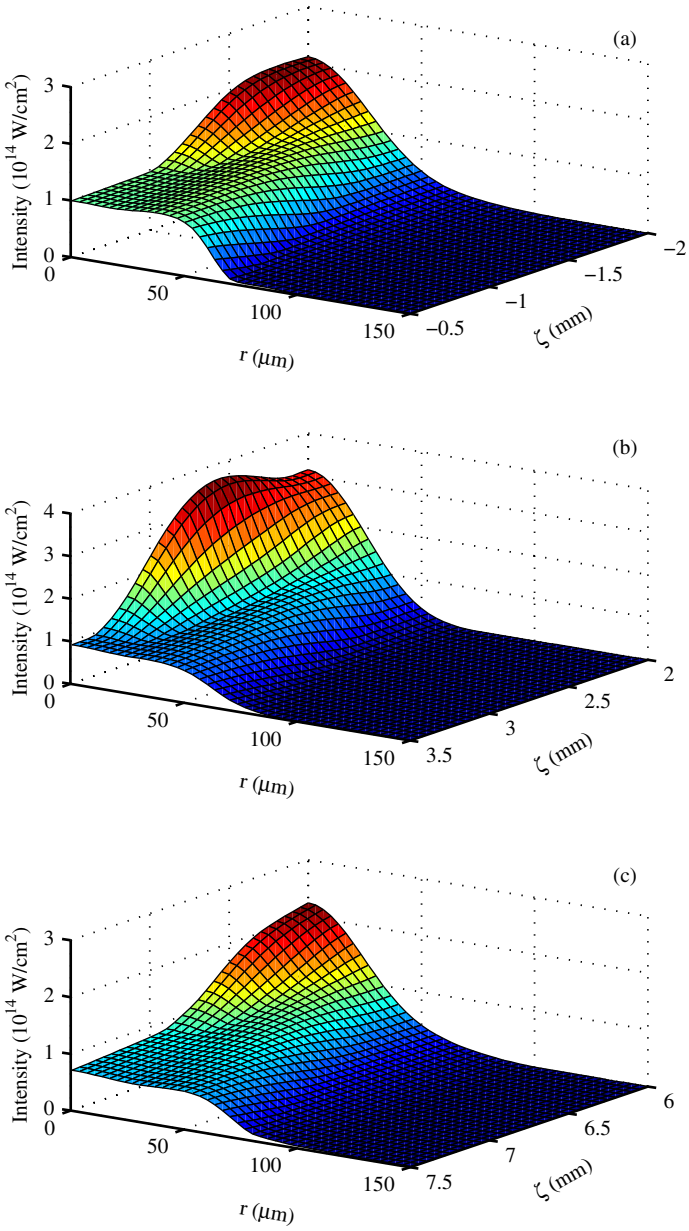

Figure 5. Spatial configuration of the laser field for three different positions of the medium entrance relative to the focus: (a) $\zeta = -2$ mm, (b) $\zeta = 2$ mm and (c) $\zeta = 6$ mm.

defocusing, the intensity of the beam can decrease even before the focus, which can lead to excellent PM conditions on the propagation axis. We emphasize here that this situation cannot occur in the case of an unperturbed Gaussian beam, but only when the beam-distorting effect of plasma defocusing is very strong.

In a diverging beam ($\zeta = 6$ mm), the flat radial profile is decreasing in intensity faster along the propagation direction as the diffraction and plasma act in the same direction. Finally, for a higher intensity ($\zeta = 2$ mm) the flat profile will be formed after a longer propagation distance.

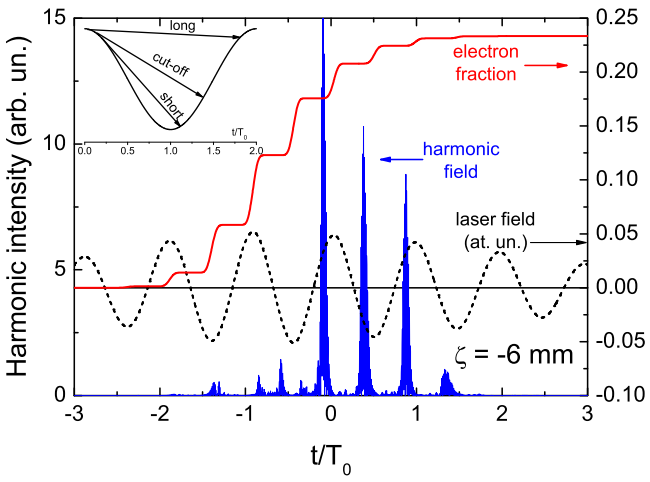

Figure 6. Time dependence of the harmonic field, laser field and the electron fraction on-axis at exit from the medium for $\zeta = -6$ mm. The right scale refers to both electron fraction and laser field in atomic units. The inset shows the short, cut-off and long trajectories in the Kramers–Henneberger frame.

For a limited extension of the gas jet, this means that the flat profile is either not formed or happens in a small volume of the interaction region. The harmonic generation finds favourable PM conditions mainly in the flat intensity region. Indeed for a large variation of intensities along both the radial and axial directions, the dipole phase will vary accordingly and thus the PM condition may occur in small confined regions. The field configuration for $\zeta = 2$ mm better illustrates this case and gives a qualitative explanation for the gap in the HH field which is observed when the gas jet is placed in the central part of the beam.

We are now in a position to analyse the HH generation in L, S and C regions shown in figure 3(a). To do this we examined for the three cases the temporal structure of the harmonic field appropriately filtered to cover the region of enhanced harmonics. The temporal structure of the harmonic field as well as the on-axis laser field at the exit from the medium is presented in figure 6 for the $\zeta = -6$ mm position (thus L region). The laser field helps us to identify the kind of trajectories which were phase-matched to generate the harmonic field. As we can see, the bursts of radiation are emitted slightly *before* the maxima (in absolute value) of the laser field, which means that the long (L) trajectories are responsible for the HH formation. The inset of figure 6 illustrates this, showing the long, cut-off and short trajectories in a frame oscillating at the field frequency (the Kramers–Henneberger frame). We mention that we additionally analysed the emitted burst at $t = 0$ in figure 6 and found that the chirp of the burst is negative, which proves once more that the long trajectory survives and gives the largest contribution to the final harmonic field. The spatial structure of the 35 eV field is shown in figure 7 and reveals that favourable field formation takes place in the last third of the medium, coinciding with the flattening region of the laser field.

Next we analyse the harmonic formation after the focal point, S region in figure 3(a) at $\zeta = 3$ mm, where both the axial and the radial variations of the driving field are faster in the flattening region as shown in figure 5(c). The time dependence of the harmonic and laser fields is shown in figure 8 and show that the bursts of radiation are emitted slightly *after* the maxima

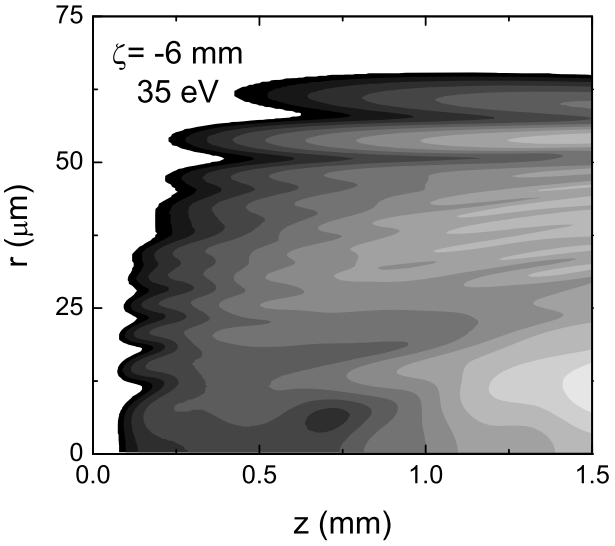

Figure 7. Spatial structure of the harmonic field at 35 eV for the medium position $\zeta = -6$ mm. The scale is in arbitrary units and spans over two orders of magnitude.

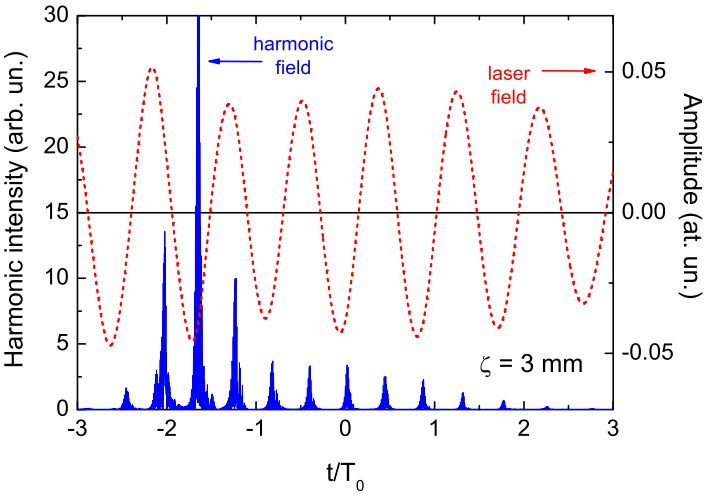

Figure 8. Time dependence of the harmonic field and laser field at exit from the medium for $\zeta = 3$ mm.

(in absolute value) of the laser field. This demonstrates that the contributing electron trajectories are short (S), which is supported also by the positive chirp found in the emitted bursts.

The spatial dependence of the 35 eV harmonics is shown in figure 9. Compared to the field in figure 7, the divergence of the field is larger as confirmed by inspecting the orientation of the contour lines defining the regions of equal intensity. This divergence originates mainly from the divergence of the laser field which is produced both by plasma defocusing and by diffraction.

The coherence length map indicates that short trajectories found better PM conditions, again in the last third of the interaction region, confirming the data in figure 8. At first sight these results may look surprising as they are contrary to what is the expected behaviour of harmonic generation as a function of medium position. The majority of results obtained at low

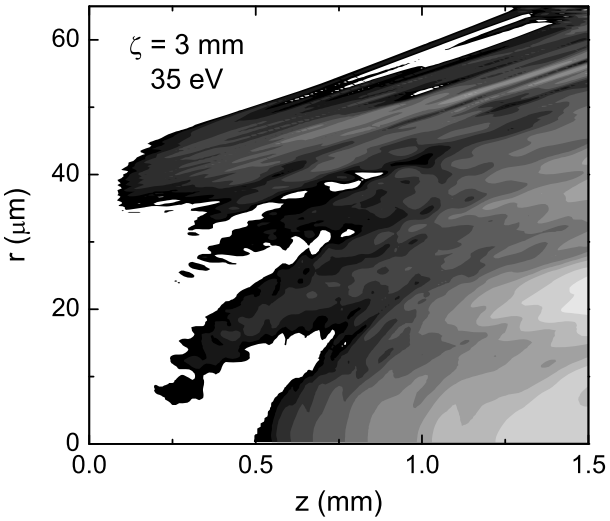

Figure 9. Spatial structure of the harmonic field at 35 eV for the medium position $\zeta = 3$ mm. The same scale as in figure 7.

ionization levels show that short trajectories survive after the focus and generate harmonics with low divergence, while the long trajectories dominate the harmonic formation with larger divergence and before the focus. Here we can explain the regime of harmonic formation by estimating the PM condition before and after the focus at $\zeta = -6$ mm and $\zeta = 3$ mm. We choose these positions because here we have intense harmonic signal at low-order harmonics, say 35 eV (see figure 3). As a first step we found the quantum trajectories which generate the harmonic field at 35 eV; then we estimated the (linear) dependence of their phases on laser intensity. We obtained (in units of 10^{-14} cm^2 W^{-1}) $\alpha_1 = -38$ and $\alpha_2 = -168$ for short and long trajectories, respectively; then we used these values to evaluate the PM condition by calculating the coherence lengths at 35 eV over the interaction region. We note here the large values obtained for α parameters for 1500 nm driving wavelength. This stronger dependence of the dipole phase on the driving intensity has consequences on the PM mechanism as we will see in the following.

In simple terms the difference between $\zeta = -6$ mm and $\zeta = 3$ mm can be explained by the different gradients of the driving field intensity along the propagation direction. Indeed, the PM condition for the qth-order harmonic can be seen as a balance between the dipole phase variation due to the driving field phase, i.e. $q\delta\varphi/\delta z$, and the variation due to the intensity gradient, i.e. $-\alpha\delta I/\delta z$. Assuming two symmetric ζ positions which experience the same driving field phase variation produced by similar plasma densities, the PM is fulfilled for long trajectories (large α values) when $\delta I/\delta z$ is smaller (before focus) and for short trajectories (smaller α values) when $\delta I/\delta z$ is larger (after focus).

Next we analyse the C region in figure 3(a), in particular the $\zeta = -2$ mm case in which we see an enhancement of harmonic field in the high energy region. We performed the same data inspection as above and the results can be seen in figure 10, where we have plotted the temporal structure of the harmonic field taken between 50 and 75 eV. Here, we see that the bursts are emitted around the zero of the driving laser field which points toward the cutoff (C)-type trajectories. One can note the shift from long toward cutoff-type electron trajectories as the bursts are emitted later within the laser pulse. For example, the burst

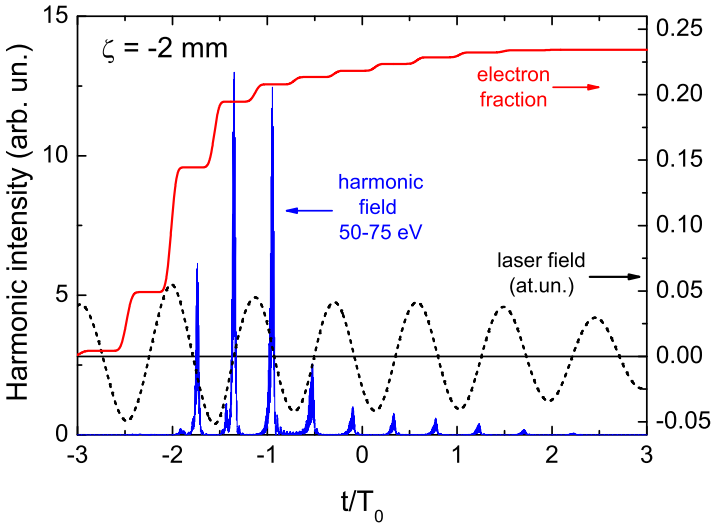

Figure 10. The same as in figure 6, but for $\zeta = -2$ mm. The time dependence of the electron fraction on-axis at medium exit is also shown. The right scale refers to both the electron fraction and laser field in atomic units.

at $t = -2T_0$ is emitted after the zero of the field, whereas at $t = -0.5T_0$ the emission happens slightly before the zero.

For this case, it is interesting to investigate the mechanism of PM, as this calculation completes the description of the process of harmonic generation at high photon energies and high ionization regime. In figure 11(a), the spatial structure of the harmonic field at 67 eV shows mainly off-axis generation but with good directionality along the propagation direction; the remaining panels show the coherence length maps. Figure 11(b) shows a time-independent PM map where the calculations were performed based on the static vector model introduced by Balcou *et al* [20], assuming slowly varying envelope and uniform phase variation of the driving pulse, without including SPM and other propagation effects. Figures 11(c)–(e) show the time-dependent coherence length for $t = -2T_0$, $t = -1.5T_0$, $t = -T_0$ and $t = -0.5T_0$, respectively. These are the optical cycles in which the most intense bursts are emitted, as seen in figure 10. The time-independent coherence length pattern has little to do with the harmonic field pattern over the interaction region. The maps at different optical cycles show more resemblance to the harmonic field map, in particular at $t = -1.5T_0$ and $t = -T_0$, where the long coherence length regions agree well with the high-intensity harmonic field region. This means that the harmonic generation at these energies is a phase-matched process which happens in a few optical cycles within the driving pulse. The high-contrast structure of harmonics observed in this spectral region (see figure 3) confirms this description. This example shows that when analysing high-ionization data the time-dependent treatment is essential in order to understand the generation mechanisms. The differences observed in figure 3 between the near and the far field can be explained by the different divergence which the harmonic field acquires for different ζ positions. In particular, the divergence is larger for ζ positions after the focus, as the laser field defocusing is more prominent. This can be inferred also from the spatial structure of the harmonic fields: for $\zeta = -6$ the field (figure 7) is more collimated along the propagation axis, whereas for $z = 3$ the field divergence is larger (figure 9). As mentioned before, in the calculation of the far field we accounted for the presence of a 1 mm diameter iris, placed 150 mm away from the jet. For

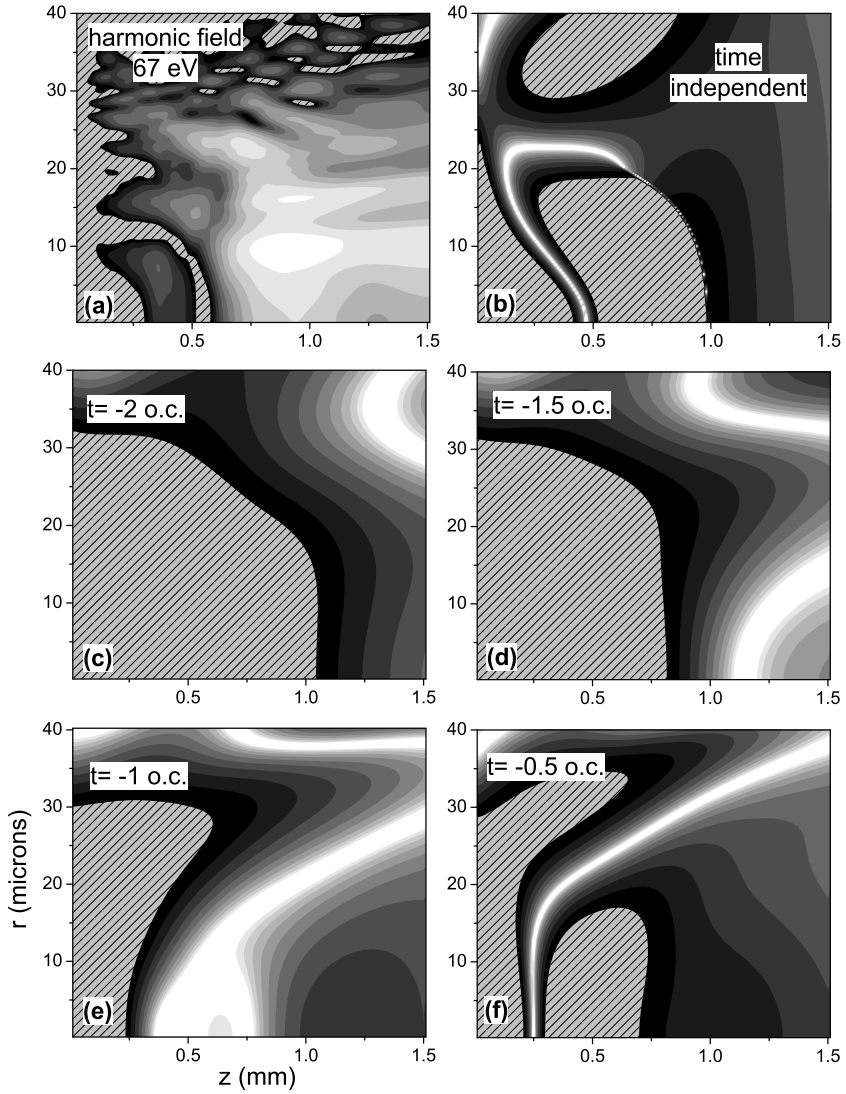

Figure 11. (a) Spatial configuration of the harmonic field generated at 67 eV. The scale is in arbitrary units and spans over two orders of magnitude. Coherence length maps for this field calculated as time-independent (b) and at different optical cycles within the laser pulse (c–f). The coherence length ranges from 0.05 mm (black) to 1 mm (light grey).

a gas jet placed after focus, we obtain better agreement between the measured spectra and the near field computed spectra, meaning that the truncation effect is less strong in the experiment. The reason could be a smaller divergence due to possible laser beam aberrations and/or due to smaller ionization levels if ADK rates overestimate the ionization.

6. Conclusions

In this paper, we presented experimental evidence for efficient XUV emission by HHG driven with mid-IR few-cycle pulses in Xe gas. The experimental results indicated that at high-photon

energies (60–70 eV) an unexpected enhancement of the harmonic signal is observable. Using a 3D non-adiabatic model, we succeeded in reproducing the experimental results and, in addition, we provided a physical explanation for the unexpected observations. We demonstrated the importance of macroscopic effects in the HHG process, such as strong beam dispersion induced by the spatio-temporal variation of the refractive index in the interaction medium due to the generated plasma, and intense SPM. These effects are shown to create favourable PM conditions which lead to the efficient production of HHs. By means of a time-dependent PM analysis we demonstrated the importance of time-dependent treatment when looking for ideal HHG circumstances in strongly ionized media, and this method provided us information on a half-optical-cycle temporal resolution.

Acknowledgments

We gratefully acknowledge F Frassetto, P Villoresi and L Poletto for the development of the XUV spectrometer. We acknowledge partial financial support from Fondazione Cariplo (project no. 2009-2562). VT acknowledges support from the European Science Foundation within the activity 'Super-intense laser–matter interactions'. VT and KK acknowledge partial financial support from FP7 project no. 221952 of ATLAS. KK is grateful for support from TAMOP-4.2.1/B-09/1/KONV-2010-0005 funded by the European Union and the European Regional Fund.

References

[1] Corkum P B 1993 *Phys. Rev. Lett.* **71** 1994–7
[2] Shan B and Chang Z 2001 *Phys. Rev.* A **65** 011804
[3] Takahashi E, Kanai T, Nabekawa Y and Midorikawa K 2008 *Appl. Phys. Lett.* **93** 041111
[4] Popmintchev T, Chen M, Cohen O, Grisham M E, Rocca J J, Murnane M M and Kapteyn H C 2008 *Opt. Lett.* **33** 2128–30
[5] Xu H, Xiong H, Zeng Z, Fu Y, Yao J, Li R, Cheng Y and Xu Z 2008 *Phys. Rev.* A **78** 033841
[6] Xiong H *et al* 2009 *Opt. Lett.* **34** 1747–9
[7] Vozzi C, Calegari F, Frassetto F, Poletto L, Sansone G, Villoresi P, Nisoli M, De Silvestri S and Stagira S 2009 *Phys. Rev.* A **79** 033842
[8] Tate J, Auguste T, Muller H G, Salieres P, Agostini P and DiMauro L F 2007 *Phys. Rev. Lett.* **98** 013901
[9] Shiner A D, Trallero-Herrero C, Kajumba N, Bandulet H-C, Comtois D, Légaré F, Giguère M, Kieffer J-C, Corkum P B and Villeneuve D M 2009 *Phys. Rev. Lett.* **103** 073902
[10] Takahashi E J, Kanai T, Ishikawa K L, Nabekawa Y and Midorikawa K 2008 *Phys. Rev. Lett.* **101** 253901
[11] Chen M C, Arpin P, Popmintchev T, Gerrity M, Zhang B, Seaberg M, Popmintchev D, Murnane M M and Kapteyn H C 2010 *Phys. Rev. Lett.* **105** 173901
[12] Calegari F, Vozzi C, Negro M, Sansone G, Frassetto F, Poletto L, Villoresi P, Nisoli M, De Silvestri S and Stagira S 2009 *Opt. Lett.* **34** 3125–7
[13] Vozzi C, Calegari F, Benedetti E, Gasilov S, Sansone G, Cerullo G, Nisoli M, De Silvestri S and Stagira S 2007 *Opt. Lett.* **32** 2975–7
[14] Vozzi C, Manzoni C, Calegari F, Benedetti E, Sansone G, Cerullo G, Nisoli M, De Silvestri S and Stagira S 2008 *J. Opt. Soc. Am.* B **25** B112–7
[15] Altucci C *et al* 1999 *Phys. Rev.* A **61** 021801
[16] Krausz F and Ivanov M 2009 *Rev. Mod. Phys.* **81** 163–234
[17] Priori E *et al* 2000 *Phys. Rev.* A **61** 063801

[18] Takahashi E, Tosa V, Nabekawa Y and Midorikawa K 2003 *Phys. Rev.* A **68** 023808
[19] Lewenstein M, Balcou P, Ivanov M Y, L'Huillier A and Corkum P B 1994 *Phys. Rev.* A **49** 2117–32
[20] Balcou P, Salieres P, L'Huillier A and Lewenstein M 1997 *Phys. Rev.* A **55** 3204–10
[21] Tosa V, Kim H T, Kim I J and Nam C H 2005 *Phys. Rev.* A **71** 063808
[22] Kung A H 1983 *Opt. Lett.* **8** 24–6
[23] Rankin R, Capjack C E, Burnett N H and Corkum P B 1991 *Opt. Lett.* **16** 835–7
[24] Kim H T, Kim I J, Lee D G, Hong K H, Lee Y S, Tosa V and Nam C H 2004 *Phys. Rev.* A **69** 031805
[25] Brimhall N, Painter J C, Powers N, Giraud G, Turner M, Ware M and Peatross J 2007 *Opt. Express* **15** 1684–9